A low-power native NMOS-based bandgap reference operating from −55°C to 125°C with Li-Ion battery compatibility

note finali covèrpage

(Article begins on next page)

03 May 2024

A low-power native NMOS-based bandgap reference operating from -55°C to 125°C with Li-Ion battery compatibility

Michele Caselli[1] | Chris van Liempd[2] | Andrea Boni[1] | Stefano Stanzione[2]

[1]Dep. of Engineering and Architecture, University of Parma, Parma, Italy

[2]imec-Holst Centre, Eindhoven, The Netherlands

Correspondence

Andrea Boni, Department of Engineering and Architecture, Univ. of Parma, Parco Area delle Scienze, 181/A, 43124, Parma, Italy. Email: andrea.boni@unipr.it

Abstract

The paper describes the implementation of a bandgap reference based on native-MOSFET transistors for low-power sensor node applications. The circuit can operate from -55°C to 125°C and with a supply voltage ranging from 1.5 V to 4.2 V. Therefore, it is compatible with the temperature range of automotive and military-aerospace applications, and for direct Li-Ion battery attach. Moreover, the circuit can operate without any dedicated start-up circuit, thanks to its inherent single operating point. A mathematical model of the reference circuit is presented, allowing simple portability across technology nodes, with current consumption and silicon area as design parameters.

Implemented in a 55-nm CMOS technology, the voltage reference achieves a measured average (maximum) temperature coefficient of 28 ppm/°C (43 ppm/°C) and a measured sample-to-sample variation within 57 mV, with a current consumption of 420 nA at 27°C.

KEYWORDS:

Bandgap Circuit, CMOS, Low-Power, Native Transistors, Wireless Sensor Node, Large Temperature Range.

1 | INTRODUCTION

Voltage reference circuits featuring small sensitivities to temperature, supply voltage, and process corner are fundamental blocks in several analog and mixed-signal integrated systems. Indeed, an accurate voltage reference is required to generate a regulated power supply with a linear or a switched voltage regulator or to set the full-scale reference of Analog-to-Digital and Digital-to-Analog converters [1,2]. In ultra-low-power systems, such as wireless sensor nodes (WSNs), autonomous circuits with energy harvesting capability [3,4], and battery-powered devices, a relevant fraction of the current consumption in stand-by mode is ascribed to the voltage reference circuit. In the last decade, there has been a major research effort to expand the application field of WSNs in harsh environments like the automotive, the industrial and the military-aerospace ones. A well known automotive wireless sensor is the tire pressure monitoring system (TPMS) [5,6], which is powered by a mechanical energy harvester. Other automotive sensors, powered by different energy harvesting (EH) techniques, have been proposed in literature [7]. Furthermore, WSNs have been introduced for leakage detection in oil or gas pipelines [8], and for monitoring the temperature and the humidity of the storage sites of missile equipment [9]. It is worth to notice that in all these WSN implementations the system is required to operate over a large temperature range (TR) extended between -55°C and 125°C.

Wireless sensors must be designed for minimum power consumption, since both tiny batteries and energy harvesters can deliver

a very limited amount of energy, and to limit the cost of the periodical battery replacement. Therefore, bandgap circuits featuring a large TR, a low power consumption, and an adequate temperature coefficient (TC) are required to expand the applicability of the WSNs in the mentioned fields.

A reference voltage circuit achieves a low TC by combining two voltages being, respectively, proportional (PTAT) and complementary (CTAT) to the absolute temperature (T). In bipolar junction transistor (BJT) bandgap references, both the PTAT and CTAT voltages are generated by means of p-n junctions[10,11], whereas in hybrid bandgaps the PTAT voltage is generated by MOS devices, possibly combined with resistors[12,13,14]. Instead, in a MOS reference, both CTAT and PTAT voltages are generated by MOS transistors[15,16].

In the last decades, several design techniques have been investigated to reduce the minimum supply voltage of the bandgap circuit. Moreover, in Internet-of-things (IoT) applications the use of advanced process nodes is getting common to achieve both power saving and a smaller area of the digital core. However, the breakdown voltage of the thick-oxide devices in the sub-100-nm nodes is usually between 3.3 V and 1.8 V, with relevant design issues to extend the voltage supply up to 4.2 V. Indeed, this voltage would allow the bandgap reference to be directly attached to a Li-Ion battery, as often required in the power management units (PMU).

Remarkable research activity has been also carried out to push the power consumption of voltage references in the hundreds of pW range[15,12,17], by exploiting the leakage current of a MOS device to bias the circuit[15,16,18,14,19]. However, these architectures exhibit small operative TRs due to the high variability of the bias current, which becomes too small to mantain target performance at low temperatures.

In a bandgap reference, the presence of an additional operating point, usually corresponding to the zero-bias condition, requires a dedicated start-up circuit (SUPC), which, at the power-on, pushes the circuit bias far from the undesired operating condition[20,21]. The most common SUPC implementations belong to three main categories. In the first category (type-1 SUPC) a start-up device, either an NMOS[22] or a PMOS transistor[23], injects current in specific nodes of the bandgap core at the power-on. This device is driven by an inverter gate having its input controlled either by the output reference voltage or by the CTAT voltage. This inverter stops the current injection when the circuit is far from the wrong bias point, and it is usually implemented either with a PMOS load with the gate shorted to ground[22] or as a CMOS gate[24,23,25,26]. In type-2 SUPCs, a start-up current is derived from the supply voltage and injected in the bandgap core. A feedback loop is introduced to switch-off the current injection[27]. In type-3 SUPCs, the inverter is replaced by a POR generator, based on a current generator mirroring the bias current of the bandgap core[28]. It is worth noticing that SUPCs of the first type exhibit a significant dependence of the inverter threshold with the supply voltage, whereas in type-2 SUPCs the start-up current increases with the supply voltage.

Therefore, in the majority of the SUPCs, two main issues stand: proper start-up operations at low voltage supplies and proper deactivation of the SUPCs at high voltage supplies. Achieving both features can be very challenging if the application requires a wide supply range.

Moreover, if the supply voltage exceeds the gate-source voltage limit of the MOS devices a major issue occurs at the power-on when some transistors in the bandgap core may undergo significant over-voltage stress, leading to drift of the reference voltage. This situation is common to many SUPCs with some internal nodes forced, at the power-on, to a voltage close either to the supply or to ground. Summarizing, start-up free bandgap circuits, featuring a single operating point, are preferred when the target application requires a wide temperature range, a large supply voltage range, and a sub-microampere current consumption.

This paper presents a hybrid voltage reference, based on native NMOS (N-NMOS) transistors in 55-nm CMOS. N-NMOS devices exhibit a negative threshold voltage and are generally available in modern silicon technologies[16,29,30]. The proposed voltage reference operates on a TR of 180°C, a supply range from 1.5 V to 4.2 V, with a current consumption in the hundreds-nanoamperes range. A typical TC of 28 ppm/°C was measured. To the best of authors' knowledge, this is the first bandgap reference that is fully compliant with the military-aerospace temperature range, with a current consumption lower than 500 nA. The circuit is biased with a PTAT current, which is strongly desensitized to the MOS process tolerance. In addition, the proposed reference circuit exhibits a single bias point, thus eliminating the need for a SUPC and enabling wide operating ranges for both supply voltage (up to 4.2 V) and temperature. Finally, this paper proposes a simple mathematical model that allows the design optimization for power consumption, noise, and silicon area. The lack of simple design equations enabling easy portability across technology nodes is a further limitation of some leakage-based reference generators[18,31].

The paper is organized as follows. In Section 2.1 the fundamental equations of the proposed bandgap are discussed, whereas the absence of additional bias points is demonstrated in Section 2.2 and the curvature affecting the output voltage is analyzed in Section 2.3. In Section 2.4 the complete circuit diagram of the proposed bandgap is presented, and in Section 2.5 the noise

model of the circuit is discussed. The measurement results on the silicon samples in 55-nm technology and a comparison with the state-of-the-art bandgap circuits are reported in Section 3.

2 | NATIVE NMOS-BASED BANDGAP ARCHITECTURE

The circuit diagram of the basic Native-NMOS based bandgap (NBB) is shown in Figure 1. Here, two matched N-NMOS devices with the same aspect ratio W/L, i.e. M_1 and M_2, have their gates shorted to ground. The drain currents I_{N1} and I_{N2} depend on the aspect ratio of M_1 and on the value of resistors R_A and R_B. By means of the current mirror made by enhanced-type PMOS M_3 and M_4, the difference between I_{N1}, multiplied by the mirror gain, and I_{N2} is routed to the branch with a polysilicon resistor, R_G, and a substrate pnp BJT, Q_1, connected in series. If M_1 and M_2 are biased in the weak-inversion (W.I.) region, I_{BG} exhibits an approximate PTAT behavior. Therefore, the sensitivity of V_{BG} to T is canceled at a reference temperature, T_0, by proper sizing of R_G.

2.1 | Circuit Analysis

An analytic expression of I_{BG} is obtained starting from the voltage balance equation of the loop involving the gate-source terminals of M_1 and M_2, together with resistors R_A and R_B:

$$\Delta V_{GS} \equiv V_{GS2} - V_{GS1} = I_{N1} R_A - I_{N2} R_B \tag{1}$$

where $V_{GS<i>}$ is the gate-source voltage of $M_{<i>}$. If M_1 and M_2 are biased in W.I., the approximate expression of the drain current is[32]:

$$I_{N<i>} = I_{SS} \cdot \left(\frac{W}{L} \right)_{<i>} \cdot e^{\frac{V_{GS<i>} - V_{TN}}{n_n \cdot v_{th}}}$$
$$\cdot \left(1 - e^{-\frac{V_{DS<i>}}{v_{th}}} \right) \tag{2}$$

where $V_{DS<i>}$ and $(W/L)_{<i>}$ are the drain-source voltage and the aspect ratio of $M_{<i>}$, respectively, v_{th} is the thermal voltage, i.e. $v_{th} = kT/q$, with q and k corresponding to the electron charge and the Boltzmann constant respectively, V_{TN} and n_n are the threshold voltage and the slope factor, and I_{SS} is the saturation current with $W/L=1$. Limiting the analysis to the case with $V_{DS1} \gg v_{th}$, ΔV_{GS} exhibits the following dependence on the temperature:

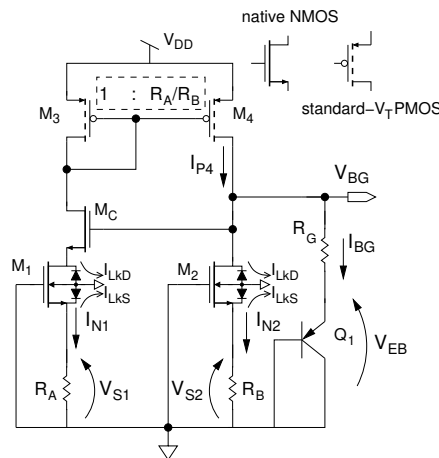$$\Delta V_{GS} \equiv V_{GS2} - V_{GS1} = n_n v_{th} \ln \left(\frac{I_{N2}}{I_{N1}} \right) \tag{3}$$

FIGURE 1 Schematic of the NBB voltage reference.

whereas, from (1), a relationship between the drain currents and the values of R_A and R_B is obtained:

$$\frac{I_{N2}}{I_{N1}} = N \cdot \left(1 - \delta_V\right) \tag{4}$$

where

$$N \equiv \frac{R_A}{R_B} \quad \text{and} \quad \delta_V \equiv \frac{\Delta V_{GS}}{V_{S1}} \tag{5}$$

Therefore, (3), is rewritten as:

$$\Delta V_{GS} = n_n\, v_{th}\, ln\left[N \cdot \left(1 - \delta_V\right)\right]$$
$$\approx n_n \cdot v_{th}\, \left[\ln(N) - \delta_V\right] \tag{6}$$

where δ_V is temperature-dependent, as will be discussed in Section 2.3. From (3) and (4) the following equations are written to obtain an analytic expression for I_{BG}:

$$I_{N1} = \frac{I_{N2}R_B + \Delta V_{GS}}{R_A} \tag{7}$$

$$I_{P4} = N\, I_{N1} \tag{8}$$

$$I_{BG} = I_{P4} - I_{N2} \tag{9}$$

Thus, replacing ΔV_{GS} in (7) with (6), the following expression is obtained from (9):

$$I_{BG} \approx \frac{N\, n_n\, v_{th}}{R_A} \cdot \left[\ln(N) - \delta_V\right] \tag{10}$$

Therefore, I_{BG} is PTAT, if the circuit is sized for $\delta_V \ll \ln(N)$. From (3), (4), and (5) this condition is rewritten as:

$$V_{S1} >> n_n\, v_{th} \tag{11}$$

Hence, the PTAT dependence of I_{BG} requires a negative V_{GS} for M_1 (and M_2). Therefore, MOS devices with a negative threshold voltage are mandatory to avoid the deep sub-threshold bias, where the simulation models are inaccurate, the current is extremely low, and, consequently, the channel noise is very high. The output voltage V_{BG} is the superposition of the PTAT voltage across R_G and the base-to-emitter voltage of Q_1, V_{EB}, which is CTAT.

$$V_{BG} = V_{EB} + \frac{N\, n_n\, v_{th}\, R_G}{R_A} \cdot \left[\ln(N) - \delta_V\right] \tag{12}$$

The value of R_G leading to a zero-TC of V_{BG} at T_0 is obtained by derivation vs. temperature of (12):

$$R_G \approx -\left(\frac{\partial V_{EB}}{\partial T}\right)_{T_0} \cdot \frac{q\, R_A}{N\, n_n\, k\, \ln(N)} \tag{13}$$

where δ_V has been neglected.

The N-NMOS M_C is added to keep the drain voltages of M_1 and M_2 almost equal and to desensitize their difference from the supply voltage. The supply sensitivity of V_{BG} is due to the variation of I_{BG} with V_{DD}:

$$\frac{d\, V_{BG}}{d\, V_{DD}} \approx R_G\, \frac{d\, I_{BG}}{d\, V_{DD}} \tag{14}$$

where the sensitivity of V_{EB} has been neglected due to its log-dependence on I_{BG}. Since the drain voltage of M_2 is equal to V_{BG}, the sensitivity of I_{N2} is negligible with respect to I_{N1}, therefore $d\, I_{BG}/d\, V_{DD} \approx d\, I_{P4}/d\, V_{DD}$.

The dependence of I_{P4} on V_{DD} is due to the finite output resistance of the M_3-M_4 mirror and to the dependence of I_{N1} on V_{DS1} from (2). Neglecting the supply-dependence of the gate voltage of M_C, the sensitivity of I_{P4} to V_{DD} with M_C becomes:

$$\frac{d\, I_{P4}}{d\, V_{DD}} \approx N \cdot \left(\frac{n_n\, v_{th}}{V_{AN}}\right)^2 \cdot \frac{1}{L_1\, L_C} \cdot \frac{1}{R_A} + \frac{N\, I_{N1}}{V_{AP}\, L_4} \tag{15}$$

where V_{AN} and V_{AP} are the normalized Early voltages [33]. If the calculation is repeated without M_C, it is found that M_C reduces the line sensitivity of I_{P4} and V_{BG} by a factor $\left(V_{AN}\, L_C\right)/\left(n_n\, v_{th}\right)$.

A mandatory feature of any analog cell to be used in a low power system is the ability to be driven in power-down condition. In the circuit of Figure 1, the presence of N-NMOS devices, which requires a negative gate-to-source voltage to limit their drain current at the level of the leakage current, raises some design issue. The power-down condition can be achieved by introducing a PMOS switch that shorts the gate of M_3 and M_4 to the supply. Thus, switching off the PMOS current mirror at the top of the

circuit in Figure 1 guarantees that the current through the right branch, i.e. M_4, M_2, and R_B, and through Q_1 is reduced to the leakage current. The left branch requires an additional NMOS switch placed in series to R_A to inhibit the current flow through N-NMOS M_C. The value of R_A in the megaohm range makes negligible the effect of the series resistance of the additional NMOS switch on the bandgap behavior.

2.2 | Self Start-up analysis

Several bandgap architectures[34,13,35,36,20] are based on a feedback loop where an amplifier sets the bias current injected in a couple of nodes to null their voltage difference. This circuit technique usually leads to an additional bias point with almost zero current, thus forcing the adoption of a dedicated SUPC[21]. The proposed bandgap reference is, by design, free from the undesired bias point, since the current is set by a pair of N-NMOS devices with the gate tied at the ground potential. Indeed, an N-NMOS device, with a negative threshold voltage and with $V_{GS} = 0$, is biased in the moderate (M.I.) or even in the strong inversion (S.I.), depending on the value of V_{TN}. In the circuit of Figure 1, at the start-up, $I_{N1}=I_{N2}=0$ and, consequently, $V_{S1}=V_{S2}=V_{BG}=0$. As soon as the voltage at the drain of M_C reaches a few thermal voltages, M_C is biased in the M.I. or S.I. and saturation due to its negative V_{TN}. Since I_{P4} is linked to the drain current of M_C, the output voltage V_{BG} rises, while the drain voltage of M_1 follows the V_{BG} voltage, due to the unity voltage gain from the gate to the source of M_C. Therefore both M_1 and M_2 leave the linear region and are biased in M.I. or even S.I.. Afterward, the negative feedback introduced by R_A (and R_B) progressively reduces the drain current of M_1 (and M_2) until a stable bias point is reached.

It is worth noticing that in the circuit of Figure 1 a positive feedback loop involving M_C, M_3, and M_4 is present. To exclude any stability issue, the low-frequency loop gain T_C must be evaluated:

$$T_C \approx \frac{g_{mC}}{1 + g_{mC} \cdot \left(r_{ds1} + R_A \right)} \cdot \frac{R_G \, g_{m4}}{g_{m3}} \tag{16}$$

where $g_{m<i>}$ and $r_{ds<i>}$ are respectively the small-signal transconductance and drain-source resistance of $M_{<i>}$. Cosidering that in W.I. $g_{mC} \approx g_{m1}$ and the intrisic voltage gain of M_1, i.e. $g_{m1} r_{ds1}$, is expected to be much higher than unity, (16) is simplified as follows:

$$T_C \approx \frac{N \, R_G}{r_{ds1} + R_A} \tag{17}$$

Sizing M_1 with $r_{ds1} >> R_G$, will keep the value of T_C below unity over process corner and temperature range, thus leading to an inherently stable loop, with no issues at the start-up.

2.3 | Bandgap Curvature and Tolerance

A non-linear equation is obtained from (2) with M_1 in the saturation region and V_{GS1} replaced by its current-dependent expression, i.e. $V_{GS1} = -I_{N1} \cdot R_A$:

$$I_{N1} - I_{SS} \cdot \left(\frac{W}{L} \right)_1 \cdot e^{\frac{-I_{N1} R_A - V_{TN}}{n_n \cdot v_{th}}} = 0 \tag{18}$$

The analytic expressions of I_{N1} is obtained by solving (18):

$$I_{N1} = \frac{n_n v_{th}}{R_A} \cdot W\left(\alpha_L \right) \tag{19}$$

$$\alpha_L = \frac{I_{N1}^0 R_A}{n_n v_{th}} \tag{20}$$

where $W(z)$ is the Lambert's W function solving the equation $x \cdot exp(x) = z$[37] and I_{N1}^0 is the equivalent[1] W.I. drain current of M_1 at $V_{GS1} = 0$, i.e. calculated with (2). Following a similar procedure with $V_{GS2} = -I_{N2} \cdot R_A / N$ the expression of I_{N2} is obtained:

$$I_{N2} = N \cdot \frac{n_n v_{th}}{R_A} \cdot W\left(\frac{\alpha_L}{N} \right) \tag{21}$$

Furthermore, a design equation for $(W/L)_1$ is obtained from (2), with I_{N1} as independent variable and V_{S1} as a parameter:

$$\left(\frac{W}{L} \right)_1 = \frac{I_{N1}}{I_{SS}} \cdot e^{\frac{V_{S1} + V_{TN}}{n_n v_{th}}} \tag{22}$$

---

[1]With $V_{TN} < -4 \cdot v_{th}$ the N-NMOS device is in S.I. at $V_{GS} = 0$ and, hence, the effective drain current will differ from I_{N1}^0.

From (11), $V_{S1}/(n_n v_{th})$ is expected to be large. Thus if a bias current in the tens-to-hundreds nA range is required, a large aspect ratio for M_1 is called for, in the case of slightly negative V_{TN} and a typical value for I_{SS}.

The tolerance affecting I_{N1} and I_{N2} at some T is mainly ascribed to R_A and n_n, since the W(x) function exhibits a small derivative at high values of x. Hence, the sensitivity of I_{N1} to I_{N1}^0, i.e. to the MOS process corner, is strongly attenuated. Therefore, with respect to leakage-based references [15,13,14,18,38,16], the proposed circuit exhibits a much smaller variation of the bias current over the MOS corner space. Furthermore, the mismatch and process tolerance affecting R_A and R_B cause a negligible deviation from the PTAT behavior, as proved by simulations and experimental results. Table 1 reports the values of the normalized sensitivities of I_{N1} and I_{BG} to $k_n \equiv \mu_n C_{OX}$, V_{TN}, and n_n, for the NBB reference:

$$S_{kn} \equiv \frac{\partial I_{N1}}{\partial k_n} \cdot \frac{k_n}{I_{N1}} \quad , \quad S_{nn} \equiv \frac{\partial I_{N1}}{\partial n_n} \cdot \frac{n_n}{I_{N1}} \quad , \quad S_{VTN} \equiv \frac{\partial I_{N1}}{\partial V_{TN}} \cdot \frac{V_{TN}}{I_{N1}} \tag{23}$$

$$S_{kn}^{BG} \equiv \frac{\partial I_{BG}}{\partial k_n} \cdot \frac{k_n}{I_{BG}} \quad , \quad S_{nn}^{BG} \equiv \frac{\partial I_{BG}}{\partial n_n} \cdot \frac{n_n}{I_{BG}} \quad , \quad S_{VTN}^{BG} \equiv \frac{\partial I_{BG}}{\partial V_{TN}} \cdot \frac{V_{TN}}{I_{BG}} \tag{24}$$

$$\tag{25}$$

Two technology cases were considered (55 nm and 65 nm) in the sensitivity analysis in Table 1. The former exhibits a threshold voltage close to zero, i.e. $V_{TN} \approx$-55 mV, and the latter a large (negative) threshold, i.e. $V_{TN} \approx$-250 mV. Both designs were sized for I_{N1}=20 nA, $V_{S1} \approx$ 330 mV, and with N=12. From the simulations, it results clearly that the lower V_{TN}, the higher the corresponding sensitivity for both currents. A relevant parameter of a bandgap circuit is the TC, which, in hybrid references, is due to the non-linearity, with respect to T, of the PTAT current, i.e. $I_{BG}(T)$, and of the CTAT voltage, i.e. V_{EB}. If the analysis is limited to the former contribution, the equation of I_{BG} is written from (19), (21), and (9):

$$I_{BG}(T) = \frac{N\, n_n\, v_{th}}{R_A} \cdot \left\{ W\left[\alpha_L(T)\right] - W\left[\frac{\alpha_L(T)}{N}\right] \right\}$$
$$+ (N-1) \cdot I_{Lk}(T) \tag{26}$$

where the substrate currents of M_1 and M_2 has been taken into account. In a MOS transistor, the drain/source-to-substrate current is ascribed to the p-n junction leakage and to the gate-induced drain leakage (GIDL) currents, i.e. $I_{Lk} = I_{LkD} + I_{LkS}$ in Figure 1,[39]. The impact ionization effect adds a further contribution [40,41,42]. Both the junction leakage and the GIDL currents exhibit an approximate exponential dependence on the temperature [40,43]. The effect is enhanced in the NBB circuit if M_1 and M_2 are sized with a large width, as from (22), since it affects the slope of $I_{BG}(T)$ at high temperature due to the higher value of $I_{LK}(T)$. Furthermore, N-NMOS devices exhibit a larger depletion width than standard-V_T devices at the same bias, due to the lower channel doping, thus leading to a higher substrate current [39]. Concerning the gate leakage, it is negligible if thick-oxide devices are used.

The increase of the first-order derivative of $I_{BG}(T)$, due to I_{Lk}, over-compensates the CTAT behavior of $V_{EB}(T)$, leading to a local minimum in the $V_{BG}(T)$ function. The effect is clearly visible in the simulation results of Figure 2, which are obtained from the design of the NBB reference in the previously considered technologies with I_{N1}=20 nA and N=12. The device models include the GIDL effect and the drain/source-to-substrate diodes. The circuits were sized with different values of R_A to operate with the same V_{S1} value (traces A and B) or with almost the same overdrive voltage for M_1 and M_2 (traces A and C). From simulation results the worst average TC is obtained with the highest V_{S1}, at the same $V_{GS1} - V_{TN}$, or with the highest V_{TN}, at the same V_{S1}. This is due to the larger width of M_1-M_2, as from (22), and, hence, to the higher leakage current.
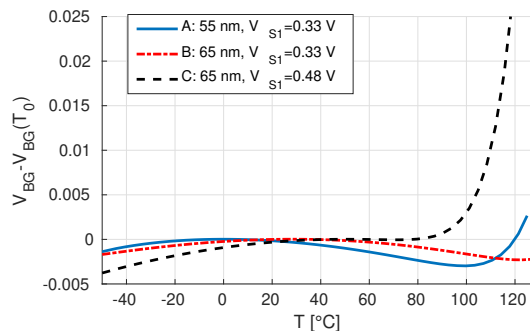

FIGURE 2 Simulated V_{BG}-$V_{BG}(T_0)$ of the NBB designed in 55 nm (V_{TH}=-55 mV) and 65 nm (V_{TH}=-250 mV) technologies.

At low-temperatures, the effect of I_{Lk} on the curvature is negligible. As shown in Appendix, Section .1, if I_{Lk} is not considered, (10) can be derived from (26) by resorting to the log-series expansion of $W(x)$[44].

Summarizing, the design equations (19), (20), and (21), shown in this section, allow a preliminary estimation of the variation of the bias current due to the process tolerance. Eq. (26) and the results shown in Figure 2 demonstrate that the minimization of the curvature of V_{BG}, in a current-constrained design, requires the optimization of the width of M_1 and M_2.

2.4 | Area and curvature optimization

In the previous section, the substrate currents of M_1 and M_2 have been identified as the cause of the local minimum of V_{BG} occurring at high temperatures. Such currents are reduced if the width of N-NMOS devices M_1 and M_2 can be reduced. This is made possible in the Threshold-Compensated NBB (THC-NBB) reference in Figure 3, where the gate voltage of M_1 and M_2, i.e. V_G, is generated by a diode-connected N-NMOS device M_5. This transistor is biased with a scaled replica of I_{N1} and is sized to operate with $V_{GS5} > 0$ V. Still in Figure 3, an option for reducing the silicon area is alos introduced. Indeed, with the current mirror M_3-M_6 the current through resistor R_A is increased, with respect to I_{N1}, by a factor equal to $(1 + K_1)$, hence reducing the value of R_A accordingly, assuming I_{N1} and V_{S1} unchanged. It is worth noticing that the area reduction is paid for by an increase in current consumption. Therefore this option should be activated if an optimum trade-off between area and current consumption is required. The current gain K_2 of the M_3-M_4 mirror must be set to:

$$K_2 = N \cdot (1 + K_1) \tag{27}$$

where $N \equiv R_A/R_B$, as for the basic NBB circuit, and K_1 is set to 0 if the low-area option (M_6 in Figure 3) is not implemented. The almost-PTAT current I_{BG} is modeled with (26), but with α_L and R_A being replaced by α_{L-C} and R_{A-C} respectively:

$$\alpha_{L-C} \equiv \frac{I_{N1-C}^0 R_{A-C}}{n_n v_{th}} \tag{28}$$

$$R_{A-C} = (K_1 + 1) R_A \tag{29}$$

where I_{N1-C}^0 is now defined as

$$I_{N1-C}^0 = I_{SS1} \left(\frac{W}{L}\right)_1 \cdot e^{\frac{V_{OV5}}{n_n \cdot v_{th}}} \tag{30}$$

The parameter V_{OV5} corresponds to the overdrive voltage of M_5, i.e. $V_{OV5} \equiv V_{GS5} - V_{TN}$. Equation (30) holds for M_5 in S.I. down to the W.I.. Using the log-series expansion of the $W(x)$ function[44], as done for (26), the approximate equation for I_{BG} is obtained:

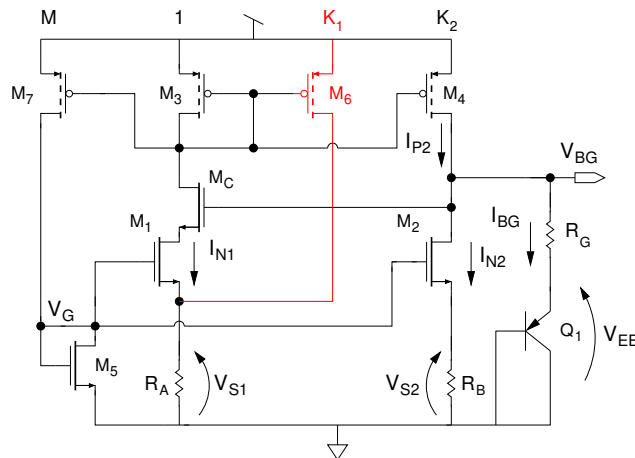$$I_{BG} \approx \frac{N n_n v_{th}}{R_A} \ln\left[(K_1 + 1) \cdot N\right] \tag{31}$$

FIGURE 3 Schematic of the THC-NBB reference. In red the optional part for area saving.

With the same procedure used for the NBB reference, a design equation for the aspect ratio of M_1 is obtained:

$$\left(\frac{W}{L}\right)_1 = \frac{I_{N1}}{I_{SS}} \cdot e^{\frac{V_{S1}-V_{OV5}}{n_n v_{th}}} \tag{32}$$

Hence, if $V_G > 0$ V, the same value of I_{N1} is obtained with a smaller width of M_1 than in the circuit in Figure 1. Since the smaller width leads to a lower substrate current, a lower average TC is expected in the THC-NBB reference in Figure 3. The local minimum, occurring for $V_{BG}(T)$ at high temperatures can be optimized by tuning the value of V_{OV5}.

Moreover, the different temperature dependence of α_{L-C} with respect to α_L must be taken into account. Indeed, the temperature behavior of I_{N1} (PTAT) and μ_n, i.e. $\mu_n(T) \propto T^{-3/2}$ [40], results in an almost PTAT behavior of V_{OV5} if M_5 is biased in S.I. and saturation:

$$V_{OV5} = \sqrt{\frac{2\,M\,I_{N1}(T)}{\mu_0\,T^{-3/2}\,C_{OX} \cdot (W/L)_5}} \propto T^{5/4} \tag{33}$$

Therefore, since $v_{th} = kT/q$, the exponent in (30) becomes almost independent of the temperature, leading to a lower variation over the temperature range of α_{L-C} compared to α_L in the NBB (i.e. without threshold compensation). It is worth noticing that in the circuit of Figure 3, a feedback loop involving M_5 has been introduced, with the potential risk of an additional bias point. Nevertheless, the drain current of M_5 is zero at the power-on and, consequently, $V_G=0$, leading to the proper start-up, as discussed in Section 2.2.

2.5 | Output Noise

The Power Spectral Density (PSD) of the output voltage noise v^2_{nBG} is calculated from the superposition of three noise sources: the BJT collector shot noise i^2_{nQ1} [45], the thermal noise voltage of R_G v^2_{nRG}, and the current noise from the MOS core generating the PTAT current i^2_{nBG}. Usually the last term is largely dominant compared with the other sources, leading to the following approximate expression:

$$v^2_{nBG} \approx R^2_G\, i^2_{nBG} \tag{34}$$

Referring to the circuit in Figure 3, the following noise sources are identified as the contributors of i_{nBG}: the channel noise of M_1-to-M_4 and M_6, the resistor noise of R_A and R_B, i.e. v^2_{nRA} and v^2_{nRB} [45], and the noise of the voltage V_G, v^2_{nG}. The noise affecting the drain current of M_1 and M_2, i.e. i^2_{n1} and i^2_{n2} respectively, is obtained by circuit analysis:

$$i^2_{n1} = \frac{i^2_{nd1} + g^2_{m1} \cdot \left(v^2_{nG} + v^2_{nRA}\right)}{\left[g_{m1}\,R_A \cdot \left(K_1 + 1\right) + 1\right]^2} \tag{35}$$

$$i^2_{n2} = \frac{i^2_{nd2} + g^2_{m2} \cdot \left(v^2_{nG} + v^2_{nRB}\right)}{\left(g_{m2}\,R_B + 1\right)^2} \tag{36}$$

where $i^2_{nd<i>}$ is the channel noise current (PSD) of $M_{<i>}$. The output noise current (PSD) due to N-MOS devices and resistors is calculated by current balance at the drain of M_2:

$$i^2_{nBG-NR} \approx \frac{K^2_2 \cdot \left[i^2_{nd1} + g^2_{m1} \cdot \left(v^2_{nRA} + v^2_{nRB}\right)\right] + i^2_{nd2}}{\left[g_{m1}\,R_A \cdot \left(K_1 + 1\right) + 1\right]^2} \tag{37}$$
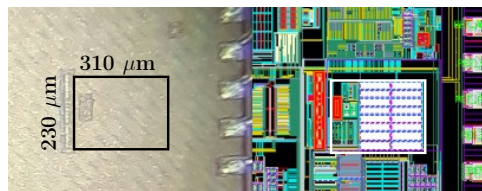

FIGURE 4 Die micro-photograph (left) and layout (right) of a part of the test-chip. The THC-NBB cell is in the black (photo) and the white (layout) rectangles.
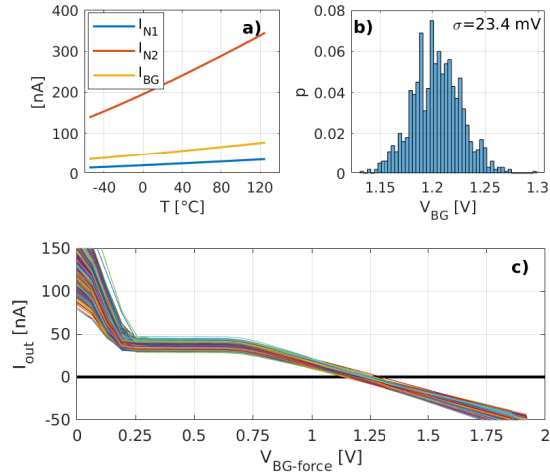
FIGURE 5 a: simulated I_{N1}, I_{N2}, and I_{BG} of the THC-NBB. b: Monte-Carlo simulation of V_{BG} at RT (y-axis is the probability of occurrency). c: Monte-Carlo search for bias points.

where the relationship between R_A and R_B, i.e. $R_B = R_A/N$, and (27) have been taken into account and assuming $\delta_V \ll 1$, thus leading to $g_{m2} \approx N\, g_{m1} \cdot (K_1 + 1)$.

The contribution of the threshold compensation circuit, i.e. v^2_{nG}, is canceled since it generates two correlated noise currents in i^2_{n1} and i^2_{n2}. The contribution of the PMOS current mirror is:

$$i^2_{nBG-P} \approx i^2_{nd4} + \left(\frac{K_2}{1 + K_1} \right)^2 \cdot \left(i^2_{nd3} + i^2_{nd6} \right) \tag{38}$$

where the approximation holds assuming $g_{m1}\, R_A \gg 1$.

Thus, the overall output noise current (PSD) is the superposition of the two contributions:

$$i^2_{nBG} = i^2_{nBG-NR} + i^2_{nBG-P} \tag{39}$$

Therefore, if $g_{m1}\, R_A \gg 1$ the PMOS devices are expected to be the most relevant noise contributors if biased in the W.I. region. The equations for the noise-driven design are reported in Appendix, Section .3.
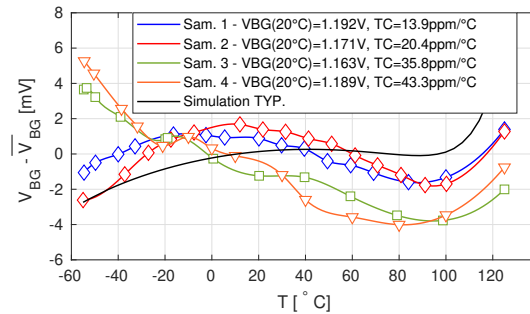

FIGURE 6 Measured V_{BG} referred to the average value of four samples. Black solid line: simulation (typical corner). The values at 20°C are reported in the legend.
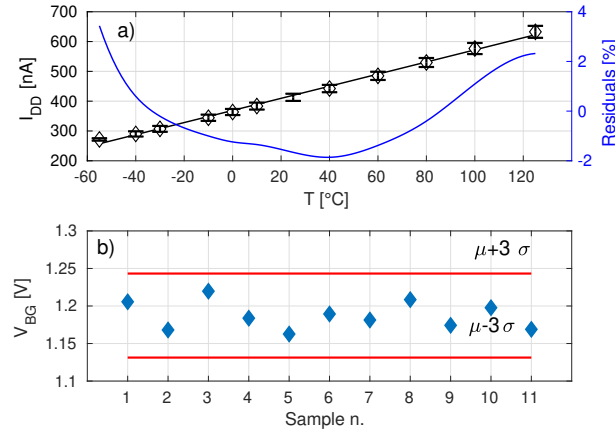
FIGURE 7 a: measured supply current and residual of the linear fitting, left and right Y-axis, respectively. Error bars show the variation over the available samples. b: output voltage of 11 samples at 30°C.
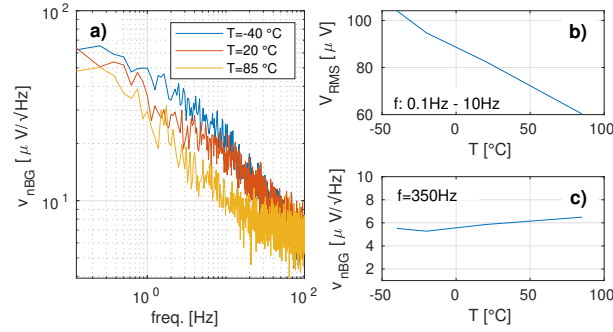

FIGURE 8 Measured noise performance. a: voltage noise spectra. b and c: low-frequency noise (rms) and PSD value in the flat region vs. temperature.

3 | EXPERIMENTAL RESULTS

3.1 | Circuit Implementation

The THC-NBB reference in Figure 3 was implemented in a 55-nm CMOS technology, Figure 4. The circuit, with a silicon area of 0.073 mm^2, was designed for the extended automotive and aerospace-military temperature range, i.e. -55°C to 125°C, with a supply voltage ranging from 1.5 V up to 4.2 V, for compatibility with Li-Ion batteries. Thick-oxide 2.5-V N-NMOS (with V_{TN}=-55 mV) and standard-V_T PMOS devices were used. The former can be over-driven up to 3.3 V of V_{GS} and V_{DS}, whereas the latter are LDMOS withstanding 3.6 V and 5.5 V of maximum V_{GS} and V_{DS}, respectively. At the maximum supply, the critical device is M_C with $V_{DSC} \approx V_{DD} - V_{SG3} - V_{BG}$. P-poly unsilicide resistors were used for R_A, R_B, and R_G with -700 ppm/°C of TC. From (12) it is clear that the resistor tolerance and temperature sensitivity affects only the V_{EB} term, which exhibits a log-dependence on I_{BG}.

Figure 5-a shows the simulated I_{N1}, I_{N2}, and I_{BG} vs. temperature for the typical process corner. The results of the Monte-Carlo simulation (process and mismatch) at RT return a standard deviation of 23.4 mV for V_{BG}, Figure 5-b. The size of the main devices of the circuit is reported in Table 2.

The presence of multiple bias points is excluded by the Monte-Carlo simulation in Figure 5-c, which shows a monotone behavior of the output current vs. the forced output voltage. This simulation was performed at the lowest temperature, corresponding to the highest threshold voltage condition.

3.2 | Measurements

Experimental measurements were performed on a set of untrimmed silicon samples, packaged in a 48-pin dual-in-line ceramic package. For the DUT characterization over temperature, we used an in-house ACS climatic chamber, featuring a maximum fluctuation of 0.3°C over the -40°C to +125°C range. For the measurement down to -55°C a Flower-ACS chamber with similar temperature stability was used. The DUT temperature was measured with a Platinum PTAT resistor (PT-100) attached to the package.

Figure 6 shows the measured voltage reference at 3.2-V supply, from -55°C to +125°C, of four samples. The average value, calculated over temperature for each sample, is subtracted from the measured V_{BG} values, to highlight the curvature. A maximum TC of 43.3 ppm/°C was measured. All the measured reference voltages show a local minimum in the range of 80°C to 100°C, in good agreement with the simulation result at a typical corner (black line). The measured reference voltages exhibit a local maximum at a lower temperature than expected from the simulation.

The measured current consumption I_{DD} vs. temperature is shown in the plot of Figure 7-a, left y-axis. An average value of 420 nA at T=27°C and V_{DD}=3.2 V is measured. The linear fitting of the measured supply current values exhibits a maximum error of about 4%. Since the supply current is equal to $I_{N1} \cdot (1 + K_1 + K_2 + M)$, the small deviation from the PTAT behavior is due to the temperature dependence of the W (α_L) term in (19). The measured tolerance of I_{DD} over the available sample population is shown by the error bar at each temperature point. Peak-to-peak variations of 3.1% and 3.0% are measured at 125°C and -40°C, respectively. Figure 7-b shows the V_{BG} value of 11 samples at 30°C. The measured mean value of V_{BG} is 1.181 V, with 1.57% of relative standard deviation, and a spread of 57 mV.

The measured power spectral density (PSD) in the low-frequency region at the low, typical, and high temperature are shown in Figure 8-a. In Figure 8-b and Figure 8-c the plots of the root-mean square (rms) value of the noise voltage in the 0.1-10 Hz range and of the power density in the white region vs. T are shown. Therefore, a positive coefficient is measured for the spectral density in the flat region, in agreement with the noise model discussed in Appendix, Section .2. The negative derivative of the low-frequency noise is ascribed to the temperature dependence of the MOS 1/f noise[53].
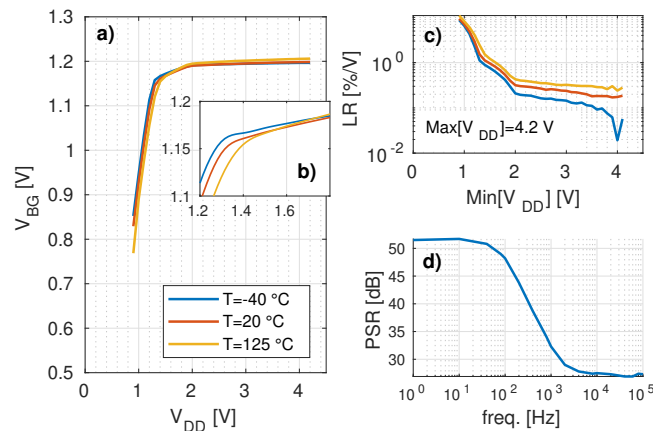

FIGURE 9 a and b: measured V_{BG} vs. V_{DD}. c: line regulation vs. minimum supply. d: PSR at 3.2-V supply.
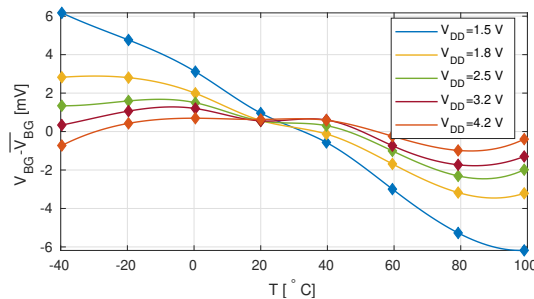

FIGURE 10 Measured $V_{BG} - \overline{V_{BG}}$ vs. temperature over the supply range.
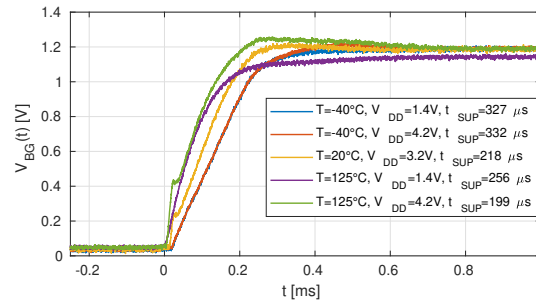
FIGURE 11 Measured V_{BG} waveforms at the power-on at different temperatures.

The variation of the voltage reference with the supply voltage, at three temperatures, is shown in Figure 9-a, with a zoomed view of the reference voltage, over a reduced supply range, in Figure 9-b. The measured line regulation for the three temperatures, is within 1%/V for a voltage supply range from 1.5 to 4.2 V, whereas it is lower than 0.6%/V and 0.3%/V with 1.8 V and 2.4 V as minimum voltage supplies, respectively.

Moreover, the measured (small-signal) power supply rejection, PSR, shown in Figure 9-d, is 52 dB at low-frequency and about 32 dB at 1 kHz, with a 3.2-V supply. The DC PSR is aligned with or better than other reported circuit implementations with a current consumption lower than 1 μA. The supply-rejection could be significantly improved with a cascode PMOS current mirror, at the cost of a smaller supply voltage range.

The measured V_{BG} of a sample vs. temperature and supply voltage is shown in Figure 10, highlighting an almost constant average TC from 3.2 V up to 4.2 V. In the lower end of the supply range the reference voltage exhibits a progressively increasing CTAT behavior. This effect is due to the supply sensitivity of I_{P4}, according to (15).

The measured start-up time, at 1% settling error, is between 200 μs and 330 μs over the supply voltage range. An on-chip shunt capacitance of 5 pF was introduced at the output. The oscilloscope waveforms are shown in Figure 11, where the supply voltage transition from 0 V to V_{DD} occurs at 0 s.
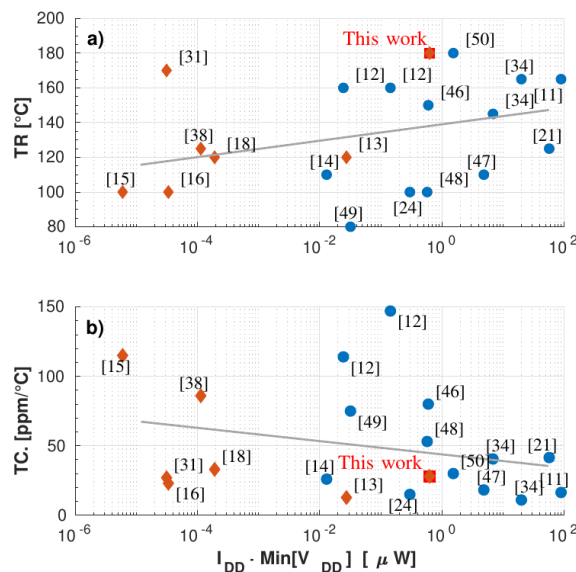

FIGURE 12 State of the art survey: blue circles: bandgaps with SUPC, orange diamonds: without SUPC, square: proposed design.

3.3 | Discussion and comments

The measured performance metrics of the proposed reference are summarized in Table 3 and compared with state-of-the-art low-power bandgap circuits, featuring a minimum supply voltage lower than 2 V [12,13,14,15,16,18,24,34,31,38,46,47,48,49,50,51,52]. Differently from the leakage-based approach [13,14], this circuit reaches a minimum operating temperature of -55°C with a 180 °C of TR, which is the largest reported in the literature at the same power consumption level. Furthermore, to the authors' knowledge, the proposed reference is the first featuring a supply voltage range from 1.5 V and up to 4.2 V, with a sub-microampere current consumption, among the silicon-proven designs reported in literature, implemented in a technology node equal or lower than 55 nm. Indeed, in [54] a bandgap reference in 28-nm technology with 5-V maximum supply is reported, but it exhibits a current consumption of 2.5 μA and a TR of only 150°C. The 28-nm PMU in [55] operates at 5 V, with a 1-μA bandgap reference, but the TR and the TC are not provided. The 5-V sub-microampere bandgap reported in [56], designed in a 180-nm technology node exhibits a temperature range of 170°C, but it is not compatible with a voltage supply lower than 2 V. The 350-nm voltage reference proposed in [57] is compatible with Li-Ion battery voltage range, but it exhibits a minimum supply voltage of 2.8 V and a temperature range of 80°C. Other N-NMOS-based bandgap circuits were reported, but none is capable to achieve our large temperature range. In [16], an N-NMOS is used for generating the bias current flowing in a stack of diode-connected PMOS devices. A power consumption of 35 pW has been achieved, but the bias current varies exponentially with the temperature, with a TR of only 100°C. In [18] and [31] N-NMOS devices are used only for cascoding purposes. The circuit in [31] achieves a TR of 170°C, but with a minimum temperature of 0°C. This severe limitation is probably a consequence of the four orders magnitude variation of the bias current over the operating TR.

The low-frequency PSR value reported in Table 3 is aligned with those of the other state-of-the-art bandgap circuits. The THC-NBB reference exhibits a comparable silicon area with the most of the other circuits in the table. The silicon occupied areas of [15,16,18,31,38,50] are approximately one order of magnitude smaller, due to the absence of high value resistors. Our bandgap circuit achieves slightly worse noise performance at room temperature than other leakage-based implementations [26,16], despite the higher current consumption. This is ascribed to the higher number of devices. Nevertheless, the white noise exhibits a relatively small dependence on the temperature, as shown in Figure 8-c. This specific feature is particularly relevant if the circuit provides the full-scale reference to an A/D or a D/A converter. Indeed, the noise affecting the reference sets an upper bound for the peak Signal-to-Noise ratio (SNR) of the converter, irrespective of its architecture. With a maximum rms noise of about 100 μV, as shown in Figure 8-c, the peak-SNR of the A/D converter is limited to approximately 78 dB. Therefore, the proposed voltage reference generator is compatible with a maximum effective resolution of 12.7 bits over the temperature range.

The scatter plots of Figure 12-a and of Figure 12-b show the TR and the TC vs. the power consumption at the minimum supply voltage [36,46,12,11,47,21,48,24,13,18,14,16,38,15,34,49,50,31]. None of the reference circuits on the left side of the graphs, hence with the lower power consumption, incorporates any SUPC, thus confirming the trend to avoid it in ultra-low power designs. It is worth to notice that our bandgap is the only one operating on a temperature range of 180°C, with power consumption lower than 1 μW. Moreover, except for [31], which exhibits a minimum temperature of 0°C, the measured mean TC is the lowest reported among the references featuring a TR larger than 120°C, and maximum power within 1 μW.

4 | CONCLUSION

A bandgap reference based on N-NMOS devices has been presented. Thanks to the novel topology, the proposed circuit operates from -55°C to 125°C, exhibits a minimum voltage supply of 1.5 V, a current consumption of 420 nA, and can be directly attached to a Li-Ion battery. The start-up circuit is not required since the proposed bandgap exhibits a single operating point. The measured TC and the limited power consumption make this circuit suitable for WSNs operating over the automotive and military-aerospace temperature range.

APPENDIX

.1 Approximation with the log-series expansion.

At high values of the independent variable x, the $W(x)$ function can be approximated by the log-series expansion[44]. The expansion, limited to the second term, gives the following equation:

$$W(x) \approx \ln(x) - \ln[\ln(x)] \tag{1}$$

Therefore, from (26) I_{BG} is approximated as:

$$I_{BG} \approx \frac{N \, n_n \, v_{th}}{R_A} \cdot \left\{ \ln(N) - \ln\left[\frac{\ln(\alpha_L)}{\ln(\alpha_L/N)} \right] \right\} \tag{2}$$

which corresponds to (10) with $\delta_V \approx \ln\left[\frac{\ln(\alpha_L)}{\ln(\alpha_L/N)} \right]$.

.2 Output noise voltage

The equation of the power spectral density of the output voltage noise is reported in (34), where the contribution of Q_1 has been neglected. The dependence of the output voltage noise on the temperature is obtained starting from the equations of $i^2_{nd<i>}$, v^2_{nRA}, and $g_{m<i>}$, assuming all MOS transistors in W.I.:

$$i^2_{nd<i>} = 2 \, q \, I_{D<i>} \tag{3}$$

$$v^2_{nRA} = 4 \, k \, T \, R_A \tag{4}$$

where $I_{D<i>}$ is the drain bias current of $M_{<i>}$. The following equation is obtained for the power spectral density of the noise voltage from (19) and (34):

$$v^2_{nBG} \approx 2 \, k \, T \, \frac{R_G^2}{R_A} \, N \, W(\alpha_L) \cdot$$
$$\left\{ \frac{2 \cdot (N+1) \, W(\alpha_L) + n_n \cdot \left[N \cdot (K_1 + 1) + 1 \right]}{\left[W(\alpha_L) + 1 \right]^2} + \right. \tag{5}$$
$$\left. n_n \cdot (N+1) \right\}$$

Since the dependence of the $W(\alpha_L)$ on the temperature can be neglected, (5) proves an approximate linear dependence of the power spectral density (in the white region) on the absolute temperature. The theoretical result is confirmed by the measurements in Figure 8-c, where the ratio of the values of v_{nBG} at 85°C and at -20°C is very close to the square-root of the ratio of the absolute temperatures.

.3 Design Optimization

In this section a set equations is presented for the automatic sizing of the main devices and currents in the THC-NBB in Figure 3. For the noise spectral density in the flat region, a useful equation is obtained from (34) with (3) and (4) in this appendix, if I_{N1} and V_{S1} are taken as independent variables. To this aim, R_A and R_G are written as:

$$R_A = V_{S1} / \left[I_{N1} \cdot (K_1 + 1) \right] \tag{6}$$

$$R_G = V_{PTAT} / I_{BG} \tag{7}$$

where V_{PTAT} is the difference between V_{BG} and V_{EB}. Then, if I_{BG} is replaced by (31) the following equation of v^2_{nBG} at RT is obtained:

$$v^2_{nBG} \approx \frac{2 \, V_{PTAT}^2 \, v_{S1}^2 \, q}{I_{N1} \cdot (K_1 + 1) \cdot \ln^2 \left[N \cdot (K_1 + 1) \right]} \cdot$$
$$\left[\frac{2 \, v_{S1} + n_n \cdot (K_1 + 1)}{n_n \cdot (v_{S1} + 1)^2} + \frac{N+1}{N} \right] \tag{8}$$

where

$$v_{S1} \equiv \frac{V_{S1}}{n_n v_{th}} \tag{9}$$

The first term within square brackets in (8) refers to the noise originated from the N-NMOS devices and resistors, whereas the second term is the contribution of the PMOS mirror. Therefore, (8) reveals that v_{nBG}^2 is inversely proportional to I_{N1} with v_{S1} constant, whereas the contribution of the N-NMOS and resistors is reduced by increasing V_{S1}.

The silicon area is approximately proportional to the sum of the values of R_A, R_B, and R_G, since it is largely dominated by the high-value resistors. Hence, the following equation for area-driven design optimization is obtained:

$$Area \approx \frac{W_R^2}{R_\square} \cdot \frac{V_{S1}}{I_{N1} \cdot (K_1 + 1)}$$
$$\cdot \left[\left(1 + \frac{1}{N}\right) + \frac{V_{PTAT}}{n_n v_{th} \ln\left[N \cdot (K_1 + 1)\right]} \right] \tag{10}$$

where W_R is the resistor width, assumed equal for all resistors in the design, and $R_\square$ is the square resistance. Referring to the schematic of Figure 3 and from (27), the current consumption of the THC-NBB circuit is:

$$I_{DD} = I_{N1} \cdot \left[(K_1 + 1) \cdot (N + 1) + M \right] \tag{11}$$

Therefore, (2), (11), (8), and (10) allow the global design optimization for current consumption, area, noise voltage, and PTAT error.

As design example of the THC-NBB in Figure 3, the following design targets are given: I_{DD}=420 nA, $v_{nBG} \approx 7 \ \mu V/\sqrt{Hz}$, and Area≈0.075 mm². The technology parameters are $R_\square$=2 kΩ and W_R=2 μm with I_{SS}=1.85 μA and n_n=1.1 both extrapolated at $V_{GS} - V_{TN} \approx$-200 mV.

A first circuit sizing is obtained by solving (8), (10), and (11), with I_{N1}, V_{S1}, and K_1 as unknown variables. Since the problem is under determined, the values of N and V_{GS5} must be preliminary chosen. For this example, with N=3 and V_{GS5}=50 mV, the set of equations returns I_{N1}=23 nA, V_{S1}=330 mV, and K_1=3. The aspect ratio of M_1 and M_2 is therefore obtained from (32), i.e. 41 μm/μm. It is worth noticing that these results are in very good agreement with the final values, obtained by simulation tuning, shown in Table 2. The procedure can be repeated by changing the value of V_{GS5} to verify the effect on the curvature and the position of the local minimum of $V_{BG}(T)$ as discussed in Section 2.4.

The data that support the findings of this study are available from the corresponding author upon reasonable request.

References

1. El-Nozahi M, Amer A, Torres J, Entesari K, Sanchez-Sinencio E. High PSR Low Drop-Out Regulator With Feed-Forward Ripple Cancellation Technique. *IEEE Journal of Solid-State Circuits* 2010; 45(3): 565-577.

2. Paavola M, others . A Micropower ΔΣ-Based Interface ASIC for a Capacitive 3-Axis Micro-Accelerometer. *IEEE Journal of Solid-State Circuits* 2009; 44(11): 3193-3210.

3. Vullers RJM, Schaijk vR, Visser HJ, Penders J, Hoof CV. Energy Harvesting for Autonomous Wireless Sensor Networks. *IEEE Solid-State Circuits Magazine* 2010; 2(2): 29-38.

4. Caselli M, Tonelli M, Boni A. Analysis and design of an integrated RF energy harvester for ultra low-power environments. *International Journal of Circuit Theory and Applications* 2019; 47(7): 1086-1104.

5. Wang Q, Li X, Li T, Bao M, Zhou W. On-Chip Integration of Acceleration, Pressure, and Temperature Composite Sensor With a Single-Sided Micromachining Technique. *Journal of Microelectromechanical Systems* 2011; 20(1): 42-52.

6. Zimmermann T, Frey A, Schreiter M, Seidel J, Kuehne I. MEMS-based piezoelectric energy harvesting modules for distributed automotive tire sensors. In: *International Multi-Conference on Systems, Signals Devices*; 2012: 1-4.

7. Mehne P, Lickert F, Bäumker E, Kroener M, Woias P. Energy-autonomous wireless sensor nodes for automotive applications, powered by thermoelectric energy harvesting. *Journal of Physics: Conference Series* 2016; 773: 012041.

8. Ali S, Ashraf A, Qaisar SB, et al. SimpliMote: A Wireless Sensor Network Monitoring Platform for Oil and Gas Pipelines. *IEEE Systems Journal* 2018; 12(1): 778-789.

9. Wang H, Zhao S, Gao W, Wang Y. Research on Automatic Monitoring System of Missile Equipment Storage Environment. *Journal of Physics: Conference Series* 2018; 1069: 012034.

10. Widlar R. New developments in IC voltage regulators. In: *1970 IEEE International Solid-State Circuits Conference. Digest of Technical Papers*. XIII. ; 1970: 158-159.

11. Ge G, Zhang C, Hoogzaad G, Makinwa KAA. A Single-Trim CMOS Bandgap Reference With a 3σ Inaccuracy of $\pm0.15\%$ From $-40°C$ to $125°C$. *IEEE Journal of Solid-State Circuits* 2011; 46(11): 2693-2701.

12. Osaki Y, Hirose T, Kuroki N, Numa M. 1.2-V Supply, 100-nW, 1.09-V Bandgap and 0.7-V Supply, 52.5-nW, 0.55-V Subbandgap Reference Circuits for Nanowatt CMOS LSIs. *IEEE Journal of Solid-State Circuits* 2013; 48(6): 1530-1538.

13. Lee JM, Ji Y, Choi S, et al. A 29nW bandgap reference circuit. In: *2015 IEEE International Solid-State Circuits Conference - (ISSCC) Digest of Technical Papers*; 2015: 1-3.

14. Ji Y, Jeon C, Son H, Kim B, Park H, Sim J. A 9.3nW all-in-one bandgap voltage and current reference circuit. In: *2017 IEEE International Solid-State Circuits Conference (ISSCC)*; 2017: 100-101.

15. Seok M, Kim G, Blaauw D, Sylvester D. A Portable 2-Transistor Picowatt Temperature-Compensated Voltage Reference Operating at 0.5 V. *IEEE Journal of Solid-State Circuits* 2012; 47(10): 2534-2545.

16. Lee I, Sylvester D, Blaauw D. A Subthreshold Voltage Reference With Scalable Output Voltage for Low-Power IoT Systems. *IEEE Journal of Solid-State Circuits* 2017; 52(5): 1443-1449.

17. Albano D, Crupi F, Cucchi F, Iannaccone G. A picopower temperature-compensated, subthreshold CMOS voltage reference. *International Journal of Circuit Theory and Applications* 2014; 42(12): 1306-1318.

18. Ji Y, Lee J, Kim B, Park H, Sim J. A 192pW Hybrid Bandgap-Vth Reference with Process Dependence Compensated by a Dimension-Induced Side-Effect. In: *2019 IEEE International Solid- State Circuits Conference - (ISSCC)*; 2019: 308-310.

19. Park B, Ji Y, Sim JY. A 490-pW SAR Temperature Sensor With a Leakage-Based Bandgap-Vth Reference. *IEEE Transactions on Circuits and Systems II: Express Briefs* 2020; 67(9): 1549-1553.

20. Boni A. Op-amps and startup circuits for CMOS bandgap references with near 1-V supply. *IEEE Journal of Solid-State Circuits* 2002; 37(10): 1339-1343.

21. Yu C, Siek L. An Area-Efficient Current-Mode Bandgap Reference With Intrinsic Robust Start-Up Behavior. *IEEE Transactions on Circuits and Systems II: Express Briefs* 2015; 62(10): 937-941.

22. Hamouda A, Arnold R, Manck O, Bouguechal N. 7.72 ppm/°C, ultralow power, high PSRR CMOS bandgap reference voltage. In: *2013 IFIP/IEEE 21st International Conference on Very Large Scale Integration (VLSI-SoC)*; 2013: 364-367.

23. Ka Nang Leung , Mok PKT. A sub-1-V 15-ppm/°C CMOS bandgap voltage reference without requiring low threshold voltage device. *IEEE Journal of Solid-State Circuits* 2002; 37(4): 526-530.

24. Ueno K, Hirose T, Asai T, Amemiya Y. A 300 nW, 15 ppm/°C, 20 ppm/V CMOS Voltage Reference Circuit Consisting of Subthreshold MOSFETs. *IEEE Journal of Solid-State Circuits* 2009; 44(7): 2047-2054.

25. Li J, Zhang X, Yu M. A 1.2-V Piecewise Curvature-Corrected Bandgap Reference in 0.5 μm CMOS Process. *IEEE Transactions on Very Large Scale Integration (VLSI) Systems* 2011; 19(6): 1118-1122.

26. Magnelli L, Crupi F, Corsonello P, Pace C, Iannaccone G. A 2.6 nW, 0.45 V Temperature-Compensated Subthreshold CMOS Voltage Reference. *IEEE Journal of Solid-State Circuits* 2011; 46(2): 465-474.

27. Kan Liu , Yadan Shen , Yidie Ye , Lenian He . A current reference based on bandgap technology with wide input voltage range by using 0.18μm BCD process. In: *2012 IEEE International Conference on Electron Devices and Solid State Circuit (EDSSC)*; 2012: 1-2.

28. Vulligaddala VB, Adusumalli R, Singamala S, Srinivas MB. A Digitally Calibrated Bandgap Reference With 0.06% Error for Low-Side Current Sensing Application. *IEEE Journal of Solid-State Circuits* 2018; 53(10): 2951-2957.

29. Chang MH, others . A highly manufacturable 0.25μm multiple-Vt dual gate oxide CMOS process for logic/embedded IC foundry technology. In: *1998 Symposium on VLSI Technology Digest of Technical Papers*; 1998: 150-151.

30. Gupta C, others . Analysis and modeling of zero-threshold voltage native devices with industry standard BSIM6 model. *Japanese Journal of Applied Physics* 2017; 56(4).

31. Lee I, Blaauw D. A 31 pW-to-113 nW Hybrid BJT and CMOS Voltage Reference with 3.6% $\pm 3\sigma$-inaccuracy from 0 °C to 170 °C for Low-Power High-Temperature IoT Systems. In: *2019 Symposium on VLSI Circuits*; 2019: C142-C143.

32. Grotjohn T, Hoefflinger B. A parametric short-channel MOS transistor model for subthreshold and strong inversion current. *IEEE Journal of Solid-State Circuits* 1984; 19(1): 100-112.

33. Binkley DM, Hopper CE, Tucker SD, Moss BC, Rochelle JM, Foty DP. A CAD methodology for optimizing transistor current and sizing in analog CMOS design. *IEEE Transactions on Computer-Aided Design of Integrated Circuits and Systems* 2003; 22(2): 225-237.

34. Chen Y, Horng J, Chang C, Kundu A, Peng Y, Chen M. A 0.7V, 2.35% 3σ-Accuracy Bandgap Reference in 12nm CMOS. In: *2019 IEEE International Solid- State Circuits Conference (ISSCC)*; 2019: 306-307.

35. Andreou CM, Koudounas S, Georgiou J. A Novel Wide-Temperature-Range, 3.9 ppm/°C CMOS Bandgap Reference Circuit. *IEEE Journal of Solid-State Circuits* 2012; 47(2): 574-581.

36. Sanborn K, Ma D, Ivanov V. A Sub-1-V Low-Noise Bandgap Voltage Reference. *IEEE Journal of Solid-State Circuits* 2007; 42(11): 2466-2481.

37. Corless RM, others . On the Lambert W function. *Advances in Computational Mathematics* 1996; 5(1): 329–359.

38. Qing Dong , Kaiyuan Yang , Blaauw D, Sylvester D. A 114-pW PMOS-only, trim-free voltage reference with 0.26systems. In: *2016 IEEE Symposium on VLSI Circuits (VLSI-Circuits)*; 2016: 1-2.

39. Roy K, Mukhopadhyay S, Mahmoodi-Meimand H. Leakage current mechanisms and leakage reduction techniques in deep-submicrometer CMOS circuits. *Proceedings of the IEEE* 2003; 91(2): 305-327.

40. Dabhi CK, others . *BSIM4 4.8.1 MOSFET Model*. UC Berkeley Device Group; 2017.

41. Chenming Hu , Simon C. Tam , Fu-Chieh Hsu , Ping-Keung Ko , Tung-Yi Chan , Terrill KW. Hot-Electron-Induced MOSFET Degradation - Model, Monitor, and Improvement. *IEEE Journal of Solid-State Circuits* 1985; 20(1): 295-305.

42. Kamata T, Tanabashi K, Kobayashi K. Substrate Current due to Impact Ionization in MOS-FET. *Japanese Journal of Applied Physics* 1976; 15(6): 1127–1133.

43. Rosar M, Leroy B, Schweeger G. A new model for the description of gate voltage and temperature dependence of gate induced drain leakage (GIDL) in the low electric field region [DRAMs]. *IEEE Transactions on Electron Devices* 2000; 47(1): 154-159.

44. Corless RM, Jeffrey DJ, Knuth DE. A Sequence of Series for the Lambert W Function. In: *Proceedings of the 1997 International Symposium on Symbolic and Algebraic Computation*ISSAC '97. ACM; 1997; New York, NY, USA: 197–204.

45. Gray PR, Hurst P, Lewis SH, Meyer RG. *Analysis and Design of Analog Integrated Circuits*. Wiley. 5th ed. 2019.

46. Watanabe H, Ando S, Aota H, Dainin M, Yong-Jin Chun , Taniguchi K. CMOS voltage reference based on gate work function differences in poly-Si controlled by conductivity type and impurity concentration. *IEEE Journal of Solid-State Circuits* 2003; 38(6): 987-994.

47. Annema AJ. Low-power bandgap references featuring DTMOSTs. *IEEE Journal of Solid-State Circuits* 1999; 34(7): 949-955.

48. Lee KK, Lande TS, Häfliger PD. A Sub-μWBandgap Reference Circuit With an Inherent Curvature-Compensation Property. *IEEE Transactions on Circuits and Systems I: Regular Papers* 2015; 62(1): 1-9.

49. Shrivastava A, Craig K, Roberts NE, Wentzloff DD, Calhoun BH. A 32nW bandgap reference voltage operational from 0.5V supply for ultra-low power systems. In: *2015 IEEE International Solid-State Circuits Conference - (ISSCC) Digest of Technical Papers*; 2015: 1-3.

50. Annema A, Goksun G. A 0.0025mm^2 bandgap voltage reference for 1.1V supply in standard 0.16μm CMOS. In: *2012 IEEE International Solid-State Circuits Conference*; 2012: 364-366.

51. Andreou CM, Georgiou J. A 0.7V, 2.7μW, 12.9ppm/°C over 180°C CMOS subthreshold voltage reference. *International Journal of Circuit Theory and Applications* 2017; 45(10): 1349-1368.

52. Cucchi F, Di Pascoli S, Iannaccone G. Variability-aware design of a bandgap voltage reference with 0.18% standard deviation and 68 nW power consumption. *International Journal of Circuit Theory and Applications* 2018; 46(11): 1985-1999.

53. van der Ziel A. Unified presentation of 1/f noise in electron devices: fundamental 1/f noise sources. *Proceedings of the IEEE* 1988; 76(3): 233-258.

54. Neri F, Brauner T, De Mey E, Schippel C. Low-power, wide supply voltage bandgap reference circuit in 28nm CMOS. In: *2015 IEEE Jordan Conference on Applied Electrical Engineering and Computing Technologies (AEECT)*; 2015: 1-6.

55. Shi C, Duncan J, Pu Y, Liu G, Homayoun A, Attar R. An Ultralow-Power On-Die PMU in a 28-nm CMOS SoC With Direct Li-Ion Battery-Attach Capability. *IEEE Journal of Emerging and Selected Topics in Power Electronics* 2018; 6(2): 465-476.

56. Huang W, Liu L, Zhu Z. A Sub-200nW All-in-One Bandgap Voltage and Current Reference without Amplifiers. *IEEE Transactions on Circuits and Systems II: Express Briefs* 2020. Early Access.

57. Wang S, Mok PKT. An 18-nA Ultra-Low-Current Resistor-less Bandgap Reference for 2.8 V -4.5 V High Voltage Supply Li-ion-Battery-Based LSIs. *IEEE Transactions on Circuits and Systems II: Express Briefs* 2020. Early Access.

TABLE 1 Sensitivity of I_{N1} to N-NMOS model parameters

	S_{kn}	S_{VTN}	S_{nn}	S_{kn}^{BG}	S_{VTN}^{BG}	S_{nn}^{BG}
V_{TN}=-55 mV	0.12	0.16	1	18m	24m	1
V_{TN}=-250 mV	0.11	0.66	0.5	17m	0.1	0.92

TABLE 2 Component Values of the THC-NBB prototype

Device	W/L	Res	[Ω]	Param.	Value
M_1	80/2	R_A	3.6 M	K_1	3
M_2	80/2	R_B	1.2 M	K_2	12
M_5	1.4/50	R_G	12 M	M	2

TABLE 3 Performance comparison with state-of-the-art low-power untrimmed reference circuits

	TR [C°]	Min T[C°]	TC [ppm/°C]	I_{DD}[b] [nA]	V_{DD} [V]	Area [mm²]	PSR@DC [dB]	LR [%/V]	Acc 3σ [%]	SUPC	Techn. [nm]	Arch.[c]
This work	**180**	**-55**	**28**	**420**	**1.5-4.2**	**0.073**	**52**	**1**	**4.7**	**NO**	**55**	**Hyb.**
[46]	150	-50	80	600	1-3	N.A.	N.A.	N.A.	1.70	YES	N.A.	MOS
[12]	160	-40	147	120	1.2-1.8	0.029	62	N.A.	2.20	YES	180	Hyb. noRes
[12]	160	-40	114	35	0.7-1.8	0.024	56	N.A.	3.15	YES	180	Hyb. noRes
[47]	110	-20	14.78	2.7·10³	0.85-1.8	0.063	N.A.	N.A.	0.9	YES	350	MOS
[48]	100	0	53.1	500	1.15-1.3	0.028	50	0.3	3.90	YES	90	Bip.
[24]	100	-20	15	214	1.4-3	0.05	45	0.002	2.8	YES	350	MOS noRes
[13]	120	-10	12.75	25	1.1-3	0.48	54	0.198	0.60	NO	350	Hyb. lb
[18]	120	-20	33	0.192	1-1.8	0.0045	55	0.02	1.56[a]	NO	180	Hyb. noRes lb
[14]	110	0	26	9.3	1.4-1.8	0.055	46	0.08	1.29	YES	180	Hyb. lb
[16]	100	0	23	0.024	1.4-3.6	0.0025	41	0.31	2.40	NO	180	MOS lb noRes
[38]	125	-40	86	0.095	1.2-2.1	0.0049	42	0.38	5.7[a]	NO	180	MOS lb noRes
[15]	100	-20	115	0.012	0.5-3.3	0.0014	49	0.033	2.40	NO	180	MOS lb noRes
[34]	145	-20	40.51	9800	0.7-0.88	0.065	N.A.	N.A.	2.35	YES	12	Bip.
[49]	80	0	125	64	0.5-1.5	0.03	40	1.6	2.00	YES	130	Bip. SC
[50]	180	-45	30	1.4·10³	1-1.7	0.0025	N.A.	N.A.	2.40	YES	160	Hyb.
[31]	170	0	27	0.034	0.9-3.3	0.0076	N.A.	0.27	1.8	NO	180	Hyb. noRes lb
[51]	180	-60	32	3.8·10³	0.7-1.8	0.023	27	N.A.	2.3[d]	YES	180	MOS
[52]	105	-25	97	68	0.8-1.4	0.28	68	0.1	1.05	NO	180	Bip.

[a] wafer

[b] Measured at the typical supply voltage

[c] **Bip**: BJT for PTAT and CTAT, **Hyb**: MOS (PTAT)+BJT (CTAT), **MOS**: MOS for PTAT and CTAT, **noRes**: resistorless, **lb**: leakage-based, **chop.**: chopping, **SC**: switched capacitors

[d] Half max-to-min range.